

# Ionic Field Screening in MAPbBr<sub>3</sub> Crystals Revealed from Remnant Sensitivity in X-ray Detection

Agustin O. Alvarez, Ferdinand Lédée, Marisé García-Batlle, Pilar López-Varo, Eric Gros-Daillon, Javier Mayén Guillén, Jean-Marie Verilhac, Thibault Lemerrier, Julien Zaccaro, Lluís F. Marsal, Germà Garcia-Belmonte,\* and Osbel Almora\*



Cite This: *ACS Phys. Chem Au* 2023, 3, 386–393



Read Online

ACCESS |

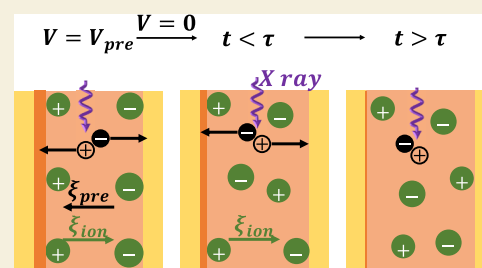
Metrics & More

Article Recommendations

Supporting Information

**ABSTRACT:** Research on metal halide perovskites as absorbers for X-ray detection is an attractive subject due to the optimal optoelectronic properties of these materials for high-sensitivity applications. However, the contact degradation and the long-term instability of the current limit the performance of the devices, in close causality with the dual electronic-ionic conductivity of these perovskites. Herein, millimeter-thick methylammonium-lead bromide (MAPbBr<sub>3</sub>) single and polycrystalline samples are approached by characterizing their long-term dark current and photocurrent under X-ray incidence. It is shown how both the dark current and the sensitivity of the detectors follow similar trends at short-circuit ( $V = 0$  V) after biasing. By performing drift-diffusion numerical simulations, it is revealed how large ionic-related built-in fields not only produce relaxations to equilibrium lasting up to tens of hours but also continue to affect the charge kinetics under homogeneous low photogeneration rates. Furthermore, a method is suggested for estimating the ionic mobility and concentration by analyzing the initial current at short-circuit and the characteristic diffusion times.

**KEYWORDS:** ion migration, X-ray detectors, metal halide perovskites, sensitivity, ion diffusion



## 1. INTRODUCTION

The use of methylammonium-lead bromide (MAPbBr<sub>3</sub>) as an absorber for X-ray detection has been established since 2016<sup>1–3</sup> thanks to the high mobility-lifetime product and small surface charge recombination velocity, which allow relatively high sensitivity (see Table S1 in the [Supporting Information](#), SI). Yet, even though the high quality of the single crystals and the thickness of polycrystals are challenging,<sup>4</sup> the instability of the contacts<sup>5</sup> and the long-term current response<sup>6–10</sup> remain arguably the key issues for the development of perovskite X-ray detectors (PXD) in general<sup>11</sup> and MAPbBr<sub>3</sub>-based devices in particular. Monitoring the photocurrent at a given reverse bias voltage with respect to the reference and stable dark saturation current is a primary requirement for typical applications in ionizing radiation imaging. Directly related to both contact degradation and long-term current evolution,<sup>12</sup> the dual ionic-electronic conductivity of these materials continues to be a puzzling subject of intensive research.<sup>13</sup>

The ionic properties of millimeter-thick perovskite samples with symmetric or rectifying contacts have been theorized in previous works.<sup>6,8–10,13–15</sup> Notably, a method for estimating ionic mobility from the short-circuit (SC) diffusion regime after bias polarization has been proposed following the ionic dynamic doping (IDD) model.<sup>6</sup> Similarly, exotic behaviors upon poling suggesting bias dependency of mobility have also been approached in the ballistic-like voltage-dependent

mobility (BVM) model. Furthermore, numerical drift-diffusion simulations of the dark saturation current of PXD have pointed out the major influence of the ionic charge field screening in biasing conditions (voltage  $V \neq 0$  V).<sup>13</sup> Yet, a description of the charge density profile and the field distributions as these samples relax toward equilibrium at SC ( $V = 0$  V) after external pre-biasing is still missing.

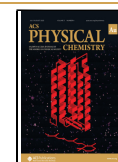
An interesting behavior has been revealed while characterizing MAPbBr<sub>3</sub> single and polycrystalline samples, as shown in [Figure 1a](#). A detailed description of the fabrication method and material characterization of similar samples can be found in previous works<sup>9,16</sup> and further specifics on our studied samples are in the experimental section S2 in the [Supporting Information](#). The general energy diagrams, with processes of charge carrier generation, recombination, and injection, are schemed and commented in [Figure S1](#) for typical photon detectors based on intrinsic semiconductor absorbers. [Figure 1b](#) shows the dark current density ( $J_{\text{dark}}$ ) and the X-ray-absorbing photocurrent ( $J_{\text{ph}}$ ) during polarization ( $V = -10$  V)

**Received:** February 17, 2023

**Revised:** April 17, 2023

**Accepted:** April 18, 2023

**Published:** May 3, 2023



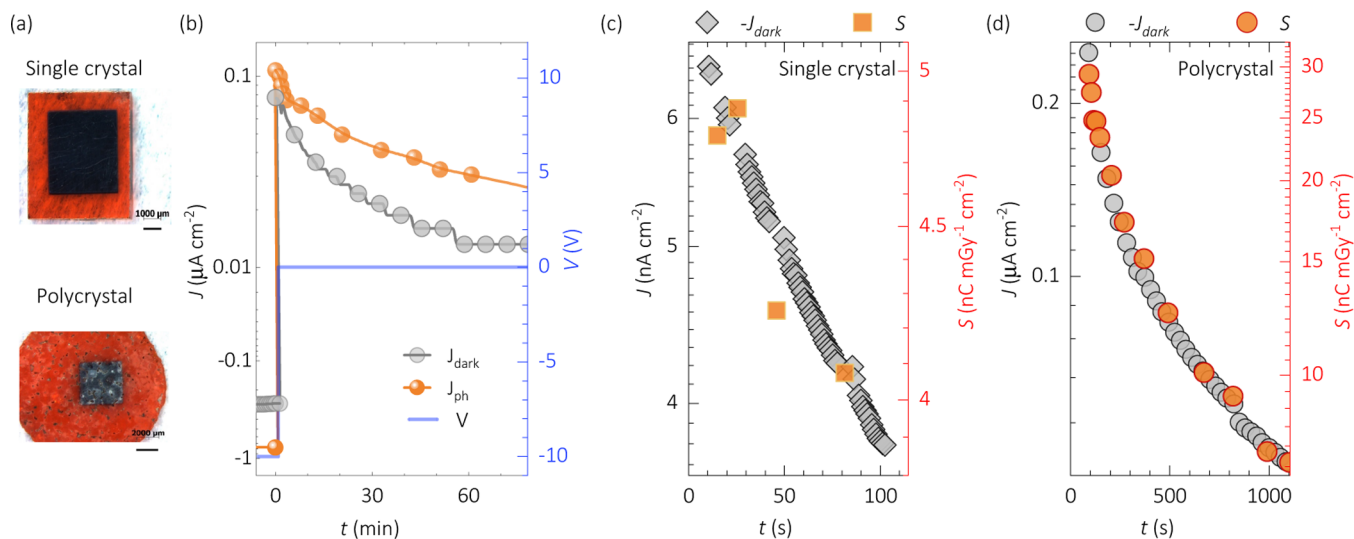


**Figure 1.** Time evolution of dark current (b–d), photocurrent (b), and sensitivity (c,d) of millimeter-thick MAPbBr<sub>3</sub> single (c) and polycrystal (b,d) samples such as those pictured in (a). The transition from biasing to the SC condition is shown in (b), while the corresponding sensitivities are in (c,d).

and the subsequent SC ( $V = 0$  V) regimes for the studied samples. During the polarization time,  $J_{\text{ph}}$  reaches values nearly three times higher than those of  $J_{\text{dark}}$ . Furthermore, no similarities in the current–time curves  $J_{\text{ph}}-t$  and  $J_{\text{dark}}-t$  during biasing were observed in our samples (neglected range in Figure 1). This could be explained due to the combination of electron injection and generation, which changes the charge mobilities and ionic–electronic concentration ratios, producing different kinetic mechanisms with respect to the dark condition. However, in the absence of injection due to external biasing (i.e., at  $V = 0$  V after biasing), the current sign is inverted, and not only is the absolute value of  $J_{\text{ph}}$  just slightly higher than that of  $J_{\text{dark}}$ , but also the corresponding  $J_{\text{ph}}-t$  and  $J_{\text{dark}}-t$  curves seem to mirror each other while transitioning from a current maximum toward equilibrium. Notably, the reproducibility of the  $J_{\text{ph}} \sim J_{\text{dark}}$  trend at SC was found regardless of the fabrication method, crystallinity, and contact materials (e.g., Cr/MAPbBr<sub>3</sub>/Cr and ITO/MAPbBr<sub>3</sub>/Cr) of the samples. This behavior is magnified in terms of the X-ray detection sensitivity ( $S$ ) for different samples of single and polycrystalline natures in Figure 1c,d, respectively. Apparently, similar sections of the dark current decay at SC produce different values of  $S$ , i.e., a higher sensitivity is reported for the polycrystalline samples over the single crystal ones. Yet, the similarity of the time evolution  $S-t$  with respect to  $J_{\text{dark}}-t$  is remarkable. This suggests that the inner field distribution caused by the mobile ion rearrangement after polarization, in the early moments of the SC regime, is not significantly changed with respect to the dark situation for small generation rates in the order of those reported in the studied samples.

In this work, the electrical response of millimeter-thick MAPbBr<sub>3</sub>-based PXD at SC after polarization is characterized and modeled. The similar time evolution of dark current and sensitivity is highlighted, and several time-dependent current–voltage experiments are conducted for attesting reproducibility. The behavior and orders of magnitudes of the electronic and ionic mobilities are explored in a set of simulations and analyzed. The simulated devices follow the Schottky–diode-like configuration from previous works,<sup>13,14,17</sup> where up-to-millimeter-thick perovskite pellets are sandwiched between

metals of different work functions (WFs). For the numerical simulations, the open-source MATLAB code Driffusion<sup>18</sup> was employed. Our results indicate the importance of interface phenomena and field screening behind the slow kinetics of thick PXDs during the diffusion regime of relaxation toward equilibrium at SC after biasing.

## 2. RESULTS AND DISCUSSION

Our first approach is to evaluate the charge carrier mobility of the samples, which will allow us to use the proper parameter ranges in the numerical simulations. Regarding the electronic (hole) mobility, the time-of-flight (ToF) current decay as a function of pulse bias is shown for single and polycrystalline samples in Figure 2a,b, respectively. As is typical in metal halide perovskite (MHP) samples,<sup>15,19</sup> there is more than one decay regime where exponential and/or power law behaviors can be argued. Nevertheless, assuming the smallest (sharpest-exponential-like region) transit time ( $\tau_{\text{ToF}}$ ), a maximum mobility can be estimated from the Mott–Gurney relation<sup>20</sup>  $\mu \cong L^2/(\tau_{\text{ToF}}V)$ , where  $L$  is the thickness of the sample. Apparently, the  $\tau_{\text{ToF}}$  between electrodes is smaller for the single crystal (1–20  $\mu\text{s}$ ) than for the polycrystalline sample (10–40  $\mu\text{s}$ ), which results in maximum mobility values ranging from 20–300 and 2–30  $\text{cm}^2 \text{V}^{-1} \text{s}^{-1}$ , respectively (see Figure 2c). The negative slope of the mobility versus voltage curve has also been previously reported in the literature for other MHPs.<sup>15,21</sup>

The impedance spectroscopy over time at SC (after pre-biasing) was measured within the framework of the IDD model<sup>6</sup> and shown for the single and the polycrystal samples in Figure 2d,e, respectively. The high resistivity of the samples (slightly higher for the single crystal sample) results in noisy spectra, yet a decreasing trend can be extracted where the resistance transits from an initial value  $R_{t_0}$  toward a saturation value  $R_{t_\infty}$ , which is typically<sup>8–10,14</sup> around 10% from the initial value, i.e.,  $R_{t_\infty}/R_{t_0} = \alpha \sim 0.1$ . Even though the stability of the contacts prevented us from measuring  $R_{t_\infty}$ , the IDD model ratio (see derivation in Section S3.1) can be rewritten as

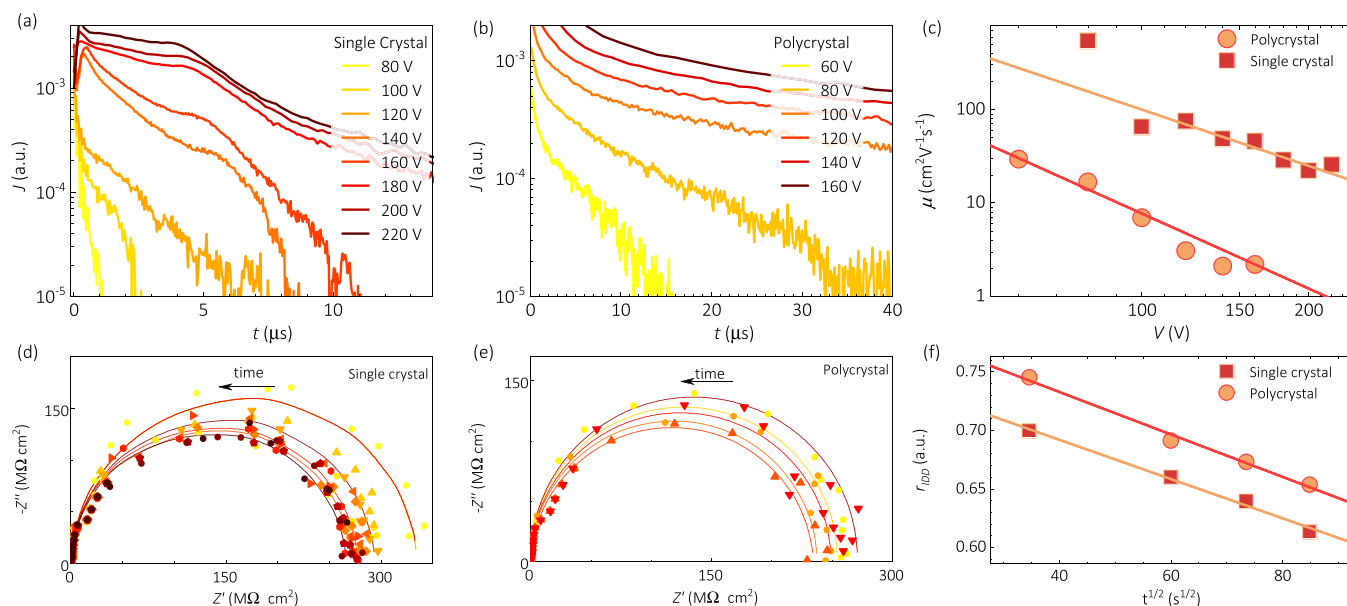


**Figure 2.** Experimental characterization of charge carrier mobility: electronic (a–c) and ionic (d–f). The time-of-flight measurements versus voltage are shown for single (a) and polycrystalline (b) samples with the corresponding maximum hole mobilities (c). The impedance spectroscopy spectra in Nyquist representation are presented for single (d) and polycrystalline (e) samples with the corresponding IDD model ratio as a function of the square root of time (f) for estimation of the ionic diffusivity. The solid lines in (c–f) indicate fittings: (c)  $\mu \propto V^{-n}$ ,  $n \sim 2$ . The full data for (a,b) is shown in Figure S4 in the SI.

$$r_{\text{IDD}} = \frac{R - R_{t0}}{R_{t0}(1 - \alpha)} = -\frac{3\sqrt{2D_{\text{ion}}t}}{L} \quad (1)$$

where the ion diffusivity  $D_{\text{ion}}$  can be used to estimate the ion mobility by means of the Einstein equation as  $\mu_{\text{ion}} = qD_{\text{ion}}/k_{\text{B}}T$ , where  $q$  is the elementary charge and  $k_{\text{B}}T$  the thermal energy (see detailed derivation in Section S3.1 of the Supporting Information). Figure 2 shows the linear behavior between the  $r_{\text{IDD}}$  and  $t^{1/2}$ , where a ratio-time slope RTS can be used to obtain  $D_{\text{ion}} = (RTS \cdot L/3)^2/2$  following the approximation of eq 1. The values resulted in  $D_{\text{ion}} \sim 2 \times 10^{-9} \text{ cm}^2 \text{ s}^{-1}$  and  $\mu_{\text{ion}} \sim 9 \times 10^{-8} \text{ cm}^2 \text{ V}^{-1} \text{ s}^{-1}$ , which agree with previous estimations in the literature.<sup>6,8–10,14</sup>

The drift-diffusion numerical simulation is a common approach among perovskite photovoltaic cells<sup>18,22–24</sup> and similar formalisms have been explored for X-ray detectors.<sup>13,25</sup> In our case, the simulation of current versus time follows the same assumptions as our previous work<sup>13</sup> at SC, as illustrated in Figure 3a–c for different previous applied voltages, mobile ion concentrations, and ion mobility, respectively. Figure 3d–f shows the corresponding initial current density  $J_0$  in each case, as well as the time  $\tau_{01}$  for which the current is 1% of the initial one, i.e.,  $J(\tau_{01})/J_0 = 0.01$ . The effect of previous bias is shown in Figure 3a,d to have no significant impact on the relaxation time, whereas the initial  $J_0$  increases linearly with the previous voltage. This suggests a typical capacitive discharge behavior, where the response time  $\tau = RC$  is affected by both the capacitance ( $C$ ) and the resistance of the sample and is independent of the charging voltage. Similarly, the higher the voltage, the higher the discharge current, in order to converge to equilibrium within the same timescale.

The effect of mobile ions in the simulated current relaxation is shown to have a major impact in Figure 3b,c,e,f. The ion concentration  $N_{\text{ion}}$  not only significantly increases the initial  $J_0$  at the same previous voltage but also decreases the relaxation time. The higher the value of  $N_{\text{ion}}$  the higher that of  $J_0$  and the

lower that of  $\tau_{01}$ . Interestingly, a clear trend  $\tau_{01} \propto N_{\text{ion}}^{-1/2}$  can be identified, whereas  $J_0 \propto N_{\text{ion}}^{1/2}$  is suggested only for specific ranges. Regarding the dependency on ion mobility  $\mu_{\text{ion}}$  (Figure 3c,f), the trends are similar but intensified in terms of the power law:  $\tau_{01} \propto \mu_{\text{ion}}^{-1}$  and  $J_0 \propto \mu_{\text{ion}}$  are apparent in the simulated range. From here, one can propose an approach similar to the ToF experiment,<sup>13</sup> but based on the effective ionic field screening  $\xi_{\text{ion}}$  created by the ions confined within the Debye length

$$L_{\text{D}} = \sqrt{\frac{\epsilon_0 \epsilon_r k_{\text{B}} T}{q^2 N_{\text{ion}}}} \quad (2)$$

where  $\epsilon_0$  is the vacuum permittivity, and  $\epsilon_r$  is the dielectric constant. Subsequently, the relaxation time can be approached by the diffusion time,  $\tau = LL_{\text{D}}/D_{\text{ion}}$ ,<sup>6,26,27</sup> and through Einstein's relation,<sup>28</sup> one can define

$$\tau_{01} = \frac{\zeta L}{\mu_{\text{ion}}} \sqrt{\frac{\epsilon_0 \epsilon_r}{N_{\text{ion}} k_{\text{B}} T}} \quad (3)$$

where  $\zeta$  is a parameterization dimensionless coefficient introduced with the definition of  $\tau_{01}$ . Similarly, the parameterization of the initial current depends on the ionic mobility and concentration. For instance, for high values of  $\mu_{\text{ion}}$  and  $N_{\text{ion}}$ , an ohmic-like behavior is obtained as a function of the previous voltage  $V_{\text{pre}}$  and

$$J_0 = \frac{q\mu_{\text{ion}} N_{\text{ion}} V_{\text{pre}}}{L} \quad (4)$$

This trend is represented with dashed lines in Figure 3d–f. However, the smaller the values of  $\mu_{\text{ion}}$  and  $N_{\text{ion}}$ , the stronger the influence of the Debye length, and thus a better description would be obtained by  $J_0 = q\mu_{\text{ion}} N_{\text{ion}} V_{\text{pre}}/L_{\text{D}}$ , which results as

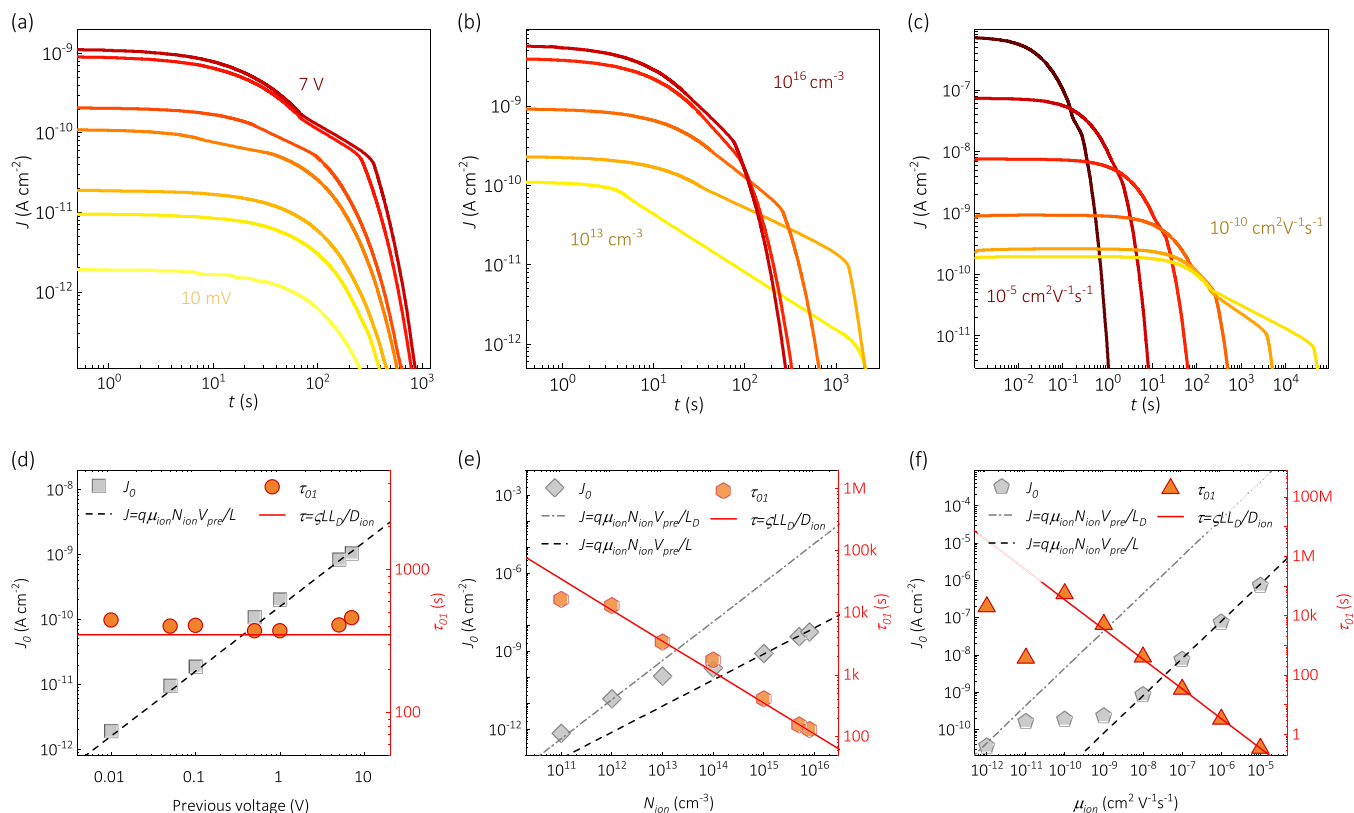


**Figure 3.** Numerical simulation of current versus time at SC ( $V = 0$  V) after biasing. The effect of different polarization biases prior to the SC regime is shown in (a), whereas the change in ion concentration and ion mobilities are shown in (b) and (c), respectively. In (d–f) are the corresponding initial currents  $J_0$  and time  $\tau_{01}$  to achieve 1% of that  $J_0$  for (a–c), respectively. Herein,  $L = 100$   $\mu\text{m}$ ,  $\mu_e = 1$   $\text{cm}^2 \text{V}^{-1} \text{s}^{-1}$ , and  $\mu_p = 10$   $\text{cm}^2 \text{V}^{-1} \text{s}^{-1}$  for (a–f);  $\mu_{\text{ion}} = 10^{-8}$   $\text{cm}^2 \text{V}^{-1} \text{s}^{-1}$  for (a,b,d,e);  $N_{\text{ion}} = 10^{15}$   $\text{cm}^{-3}$  for (a,c,d,f); previous  $V_{\text{pre}} = 5$  V for (b,c,e,f),  $\zeta = 0.5$  in (d–f).

$$J_0 = q^2 \mu_{\text{ion}} V_{\text{pre}} \sqrt{\frac{N_{\text{ion}}^3}{\epsilon_0 \epsilon_r k_B T}} \quad (5)$$

This is represented with dot-dashed lines in Figures 3e,f and S5. Notably, the transition between the transport regimes (TTR) expressed by eqs 4 and 5 is found for ionic properties with values smaller than  $\mu_{\text{ion}} = 10^{-9}$   $\text{cm}^2 \text{V}^{-1} \text{s}^{-1}$  and  $N_{\text{ion}} = 10^{14}$   $\text{cm}^{-3}$ . Accordingly, only samples with high or low enough concentrations would be out of the TTR range and display a linear dependence with  $V_{\text{pre}}$  whose slope would correspondingly match those of eqs 4 and 5. Experimentally, the application of these formalisms for  $J_0$  not only depends on the values of  $\mu_{\text{ion}}$  and  $N_{\text{ion}}$  and the TTR. The temperature and the stability of the contacts can also affect the current relaxation. For instance, Figure S6 in the Supporting Information shows several experimental current–time curves at SC after different  $V_{\text{pre}}$  values, where the linear behavior is similarly found only for  $V_{\text{pre}}$  larger than a threshold value that depends on the geometric and crystalline properties of each sample.

A method for estimating the mobility and concentration of mobile ions for perovskite samples, where further evidence suggests that  $\mu_{\text{ion}} > 10^{-9}$   $\text{cm}^2 \text{V}^{-1} \text{s}^{-1}$  and  $N_{\text{ion}} > 10^{14}$   $\text{cm}^{-3}$ , was already suggested in our previous work (focused on the pre-biasing period).<sup>13</sup> There,  $\mu_{\text{ion}}$  and  $N_{\text{ion}}$  were attainable by processing the slopes of the linear trends of the ionic time-of-flight  $\tau_{\text{IToF}}$  versus  $LT^{1/2}/V$  and the biased dark saturation current  $J_B$  versus  $qV/L$ . Complementarily, here, we suggest that eqs 3 and 4 can be used to analyze  $\tau_{01}$  versus  $LT^{-1/2}$  and  $J_0$  versus  $qV_{\text{pre}}/L$  from which the slopes of the linear trends would

deduce  $\mu_{\text{ion}}$  and  $N_{\text{ion}}$ . This diffusion-focused approach to the dark current at SC after biasing should deliver similar values to those of the biasing-focused method suggested in our previous work.<sup>13</sup>

The illustrative time evolution of the simulated electrostatic potential ( $\phi$ ), field ( $\xi$ ), charge density profiles (electrons,  $n$ ; holes,  $p$ ; anions,  $a$ ; and cations,  $c$ ), and the corresponding current density components (electron current density,  $J_n$ ; hole current density,  $J_p$ ; anionic current density,  $J_a$ ; and cationic current density,  $J_c$ ) are presented in Figure 4 as a function of the position  $x$  inside the perovskite. After 1 ms without external bias, the electrostatic potential distributes in a way that resembles the one-side abrupt p–n junction, with  $\phi$  behaving almost linearly in two main regions: the depletion region toward one electrode (at  $x = 0$ ) and the remaining bulk of the perovskite layer in Figure 4a. Accordingly, the initial electric field due to the ionic reordering is outlined in Figure 4b showing a nearly flat profile in the bulk, increasing by two orders of magnitude in the depletion region. The charge density distribution is presented in Figure 4c, where the initial depletion region occurs with the nearly sole distribution of fixed anions toward the left electrode while electrons, holes, and mobile cations reorder toward the bulk. The situation produces an ohmic-like main contribution of the cationic current in the early moments of the relaxation toward equilibrium at SC after biasing, as can be seen in Figure 4d. At this stage, it is clear that, even though no external bias is applied, the drift effect related to the internal ionic-related remnant field is a major contribution to the current in addition to the expected diffusion process.

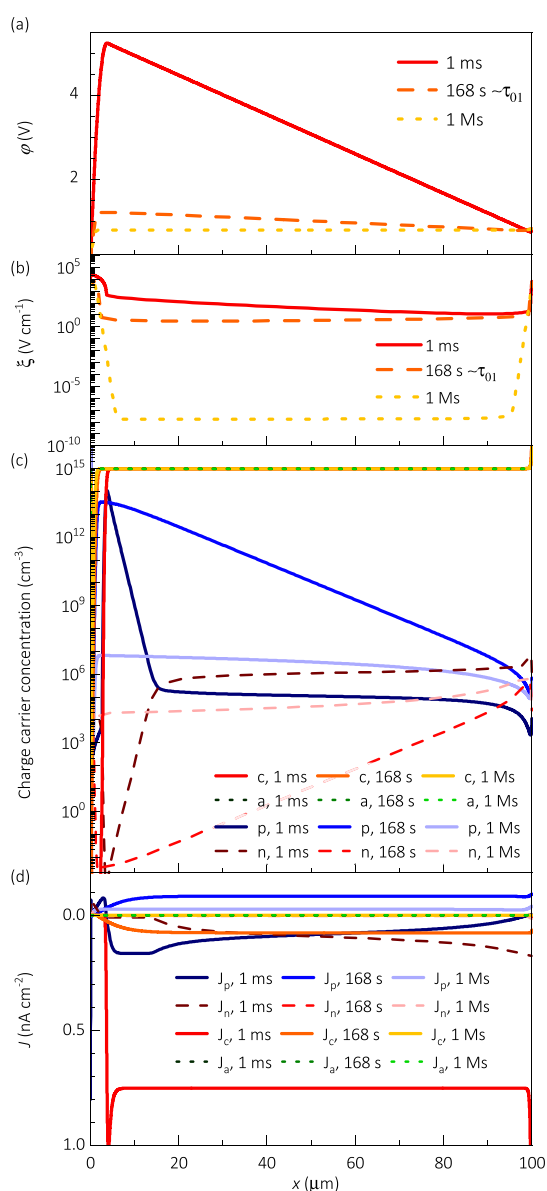


**Figure 4.** Numerical simulation of (a) electrostatic potential, (b) electric field, (c) charge density profile, and (d) current density components as a function of the position inside the perovskite at SC ( $V = 0$  V) after 5 V of previous biasing for  $\mu_{\text{ion}} = 10^{-8} \text{ cm}^2 \text{ V}^{-1} \text{ s}^{-1}$  and  $N_{\text{ion}} = 10^{15} \text{ cm}^{-3}$ .

At the characteristic diffusion time (168 s for Figure 4), most of the electrostatic potential and electric field profiles have flattened in Figure 4a,b. The consequent shrinking of the depletion layer produces an exponential gradient of electronic charge carriers in the perovskite bulk (see Figure 4c). Accordingly, not only is the diffusion electronic current in the order of magnitude of the cationic current, but it has an opposite sign that can cancel the total current or invert its sign (see Figure 4d).

In the long-term (e.g., 1 Ms  $\approx$  278 h), the electrical response approaches equilibrium at SC after biasing. Therefore, not only is the electrostatic potential practically flat, but also the electric field decreases by up to 10 orders of magnitude, as displayed in Figure 4a,b, respectively. Accordingly, the charge carrier concentration reaches a more even distribution, where no significant concentration gradients appear in the bulk, resulting

in negligible current contributions from neither the electronic nor the ionic charge carriers, as can be seen in Figure 4c,d, respectively. The longer the time at SC, after the pre-biasing, the lower the field, and thus the diffusion component becomes a principal current mechanism in the electrical response of the samples.

The previously discussed simulations for dark conditions illustrate the nature and effects of the ionic migration in the  $L_D$  region toward the interface. Subsequently, we present in Figure 5 the simulated behavior of current over time at SC after

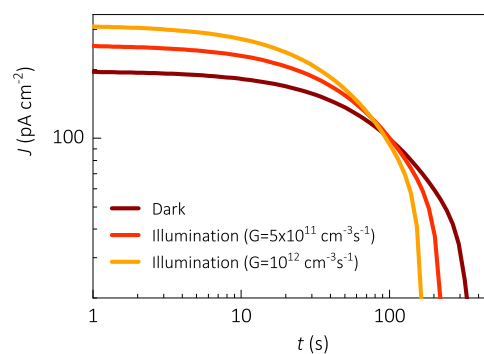


**Figure 5.** Numerical simulation of the current relaxation in the dark and under low illumination intensities with homogeneous charge carrier generation as indicated at SC ( $V = 0$  V) after 5 V of previous biasing for  $\mu_{\text{ion}} = 10^{-8} \text{ cm}^2 \text{ V}^{-1} \text{ s}^{-1}$  and  $N_{\text{ion}} = 10^{15} \text{ cm}^{-3}$ .

previous polarization for dark and homogeneous low generation rates of illuminations. Notably, this may be a rough approximation since the charge carrier generation and consequent recombination mechanisms under X-ray photon flux do not fully agree with the typical visible-to-near infrared radiation considered in the simulation code Driftfusion.<sup>18</sup> Nevertheless, our calculations suggest that, for sufficiently low generation rates, the charge density profiles and electric field distributions are not drastically changed in such a way that the photocurrent follows a general behavior very similar to that of dark conditions.

### 3. CONCLUSIONS

In summary, a set of experiments and simulations have been presented, attesting to the evidence of ionic charge-related field screening in millimeter-thick MAPbBr<sub>3</sub> single and polycrystalline samples for application in X-ray detectors. By analyzing the dark current and photocurrent under ionizing energy radiation at SC after biasing, a similar long-term relaxation trend is reported, which mirrors the sensitivity of the samples as X-ray detectors. Subsequently, the ToF and impedance spectroscopy measurements allowed us to estimate the electronic and ionic mobility in the ranges of 2–300 and  $9 \times 10^{-8} \text{ cm}^2 \text{ V}^{-1} \text{ s}^{-1}$ , respectively.

A series of simulations have been presented illustrating the effects of ionic concentration and mobility on current relaxation. It is revealed how a high internal electric field can be built upon the migration of the mobile ions when the depleting zone near an electrode during the polarization regime, prior to the relaxation to equilibrium. The tradeoff between the internal built-in and the diffusion of charge carriers is able to enhance the relaxation time by up to tens of hours, depending on the concentration and mobility of the migration ions. Purposely, for perovskite samples with  $\mu_{\text{ion}} >$

$10^{-9} \text{ cm}^2 \text{ V}^{-1} \text{ s}^{-1}$  and  $N_{\text{ion}} > 10^{14} \text{ cm}^{-3}$ , a method has been proposed for estimation of the mobility and ionic concentration based on analyzing  $J_0$  and  $\tau_{01}$  as a function of the previous voltage, distance between electrodes, and temperature.

Last but not least, we approximate the experimental comparison between dark current and X-ray photocurrent in our numerical simulations with homogeneous generation rates. It is shown how, in the proper range, the excess photo-generated electronic charge carrier densities do not produce drastic modifications to the charge balance in such a way that the currents follow similar long-term relaxation trends over time.

## 4. EXPERIMENTAL SECTION

### 4.1. Sample Fabrication

In total, 6 samples were made for this study: 2 single crystals and 4 polycrystalline films. The fabrication procedure followed the steps described in our previous work,<sup>9,16</sup> and a summary is in Section S2 of the Supporting Information. All the samples were polished prior to chromium electrode evaporation to make devices. In the symmetrically contacted samples, the top electrode (the one which receives the X-ray flux) was thinner (30 nm) than the bottom one (100 nm) in order to perform laser ToF.

### 4.2. Characterizations

The measurement of current–voltage–time characteristics was made with a Keithley 2636 B SourceMeter and a PGSTAT-30 AUTOLAB potentiostat, also used for the impedance spectroscopy measurements.

The  $J_{\text{dark}}-t$ ,  $J_{\text{ph}}-t$ , and  $S-t$  measurements were carried out with a Keithley 428 current amplifier and a Keithley 487 power supply. The samples were irradiated using a pulsed X-ray tube with an RQAS spectrum (W anode, 70 kVp, filtration: 23.5 mm Al, and 0.8 mm Be) operated at 4 Hz and 100 ms pulse duration. The incident X-ray dose was calibrated with a PTW Unidos dosimeter.  $J_{\text{ph}}$  is defined as the maximum photocurrent output for 24  $\mu\text{Gy}_{\text{air}}$  X-ray pulses. The sensitivity is calculated as the integration of  $J_{\text{ph}}$  over the pulse duration and was averaged for 10 consecutive pulses to reduce experimental error.

The measurement of laser hole ToF was made with a pulsed  $\text{N}_2$  laser with a 337 nm wavelength and an 800 ps pulse duration. The laser beam was attenuated with a neutral density filter before irradiating the samples through the top semi-transparent Cr electrode with a 30 nm thickness. A negative voltage was applied to the back Cr electrode. The ToF current waveforms were acquired with a Tektronix TDS 744A oscilloscope and a Stanford Research Systems PS310 high voltage supply.

### 4.3. Numerical Simulations

The simulations were made within the framework of Driftfusion,<sup>18</sup> as a direct continuation of our previous work on the long-term polarization regimes of thick PXDs,<sup>13</sup> including both radiative and non-radiative recombination and taking four main assumptions. First, (I) the bulk of the perovskite is initially taken as intrinsic, meaning that the total equilibrium concentrations of fixed and mobile ions should be balanced, i.e., the same total number of cations and anions (our simulation case) or effectively in the order of the intrinsic concentration (possible experimental situation). Second, (II) the interface regions between the perovskite and the contacts are unintentionally doped, forming depletion layers with thicknesses in the order of tens of nanometers. Third, (III) only one type of mobile ions is considered to effectively contribute to the current and the reordering of the charge density profile. Lastly, (IV) the built-in field forming the Schottky-diode-like detector is only defined by the difference in WF between the two metals. An illustrative set of simulation parameters is presented in Table S2, and a comprehensive explanation of the use and setting up of the Driftfusion code can be found in the original publication.<sup>18</sup>

## ■ ASSOCIATED CONTENT

### Supporting Information

The Supporting Information is available free of charge at <https://pubs.acs.org/doi/10.1021/acspchemau.3c00002>.

Introductory data on sensitivity, fabrication procedure and morphological characterization of samples, X-ray diffraction data, and simulation parameters (PDF)

## ■ AUTHOR INFORMATION

### Corresponding Authors

**Germà Garcia-Belmonte** – Institute of Advanced Materials, Universitat Jaume I, 12071 Castelló, Spain; [orcid.org/0000-0002-0172-6175](https://orcid.org/0000-0002-0172-6175); Email: [garcia@uji.es](mailto:garcia@uji.es)

**Osbel Almora** – Department of Electronic, Electric and Automatic Engineering, Universitat Rovira i Virgili, 43007 Tarragona, Spain; [orcid.org/0000-0002-2523-0203](https://orcid.org/0000-0002-2523-0203); Email: [osbel.almora@urv.cat](mailto:osbel.almora@urv.cat)

### Authors

**Agustín O. Alvarez** – Institute of Advanced Materials, Universitat Jaume I, 12071 Castelló, Spain; [orcid.org/0000-0002-0920-5390](https://orcid.org/0000-0002-0920-5390)

**Ferdinand Lédée** – Grenoble Alpes University, CEA, LETI, DOPT, F38000 Grenoble, France; [orcid.org/0000-0001-9949-0529](https://orcid.org/0000-0001-9949-0529)

**Marisé García-Batlle** – Institute of Advanced Materials, Universitat Jaume I, 12071 Castelló, Spain; [orcid.org/0000-0002-9142-2430](https://orcid.org/0000-0002-9142-2430)

**Pilar López-Varo** – Institut Photovoltaïque d'Île-de-France (IPVF), 91120 Palaiseau, France

**Eric Gros-Daillon** – Grenoble Alpes University, CEA, LETI, DOPT, F38000 Grenoble, France; [orcid.org/0000-0002-4196-7854](https://orcid.org/0000-0002-4196-7854)

**Javier Mayén Guillén** – Grenoble Alpes University, CEA, LITEN, DTNM, F38000 Grenoble, France; [orcid.org/0000-0002-2732-3809](https://orcid.org/0000-0002-2732-3809)

**Jean-Marie Verilhac** – Grenoble Alpes University, CEA, LITEN, DTNM, F38000 Grenoble, France

**Thibault Lemerrier** – Grenoble Alpes University, CNRS, Grenoble INP, Institut Néel, F38042 Grenoble, France

**Julien Zaccaro** – Grenoble Alpes University, CNRS, Grenoble INP, Institut Néel, F38042 Grenoble, France; [orcid.org/0000-0002-8150-3827](https://orcid.org/0000-0002-8150-3827)

**Lluís F. Marsal** – Department of Electronic, Electric and Automatic Engineering, Universitat Rovira i Virgili, 43007 Tarragona, Spain; [orcid.org/0000-0002-5976-1408](https://orcid.org/0000-0002-5976-1408)

Complete contact information is available at:

<https://pubs.acs.org/doi/10.1021/acspchemau.3c00002>

### Author Contributions

A.O.A.: investigation and writing-original draft; M.G-B.: investigation; P. L-V.: investigation, formal analysis, and writing—review and editing; L.F.M.: writing—review and editing and funding acquisition; G.G-B.: conceptualization, methodology, formal analysis, funding acquisition, project administration, and writing—review and editing; O.A.: conceptualization, methodology, investigation, formal analysis, writing-original draft, and writing—review and editing; J.M.: single crystal growth; T.L.: polycrystal growth; J.M.V.: materials and device fabrication; F.L.: characterization; E.G.: investigation; and J.Z.: crystal growth. CRediT: **Agustín O.**

Alvarez data curation (equal), investigation (equal), software (equal), validation (equal), visualization (equal), writing-original draft (equal), writing-review & editing (equal); Ferdinand Lédée data curation (equal), funding acquisition (equal), investigation (equal), project administration (equal), validation (equal), visualization (equal), writing-review & editing (supporting); Marisé Garcia-Battle data curation (supporting), investigation (equal), writing-review & editing (supporting); Pilar López-Varo investigation (equal), software (lead), validation (equal), writing-review & editing (supporting); Eric Gros-Daillon investigation (equal), writing-review & editing (supporting); Javier Mayén Guillén investigation (equal), writing-review & editing (supporting); Jean-Marie Verilhac investigation (equal), writing-review & editing (supporting); Julien Zaccaro investigation (equal), writing-review & editing (supporting); Lluís F. Marsal funding acquisition (supporting), writing-review & editing (supporting); Germà Garcia-Belmonte conceptualization (equal), formal analysis (equal), funding acquisition (lead), investigation (supporting), methodology (equal), project administration (lead), resources (lead), supervision (lead), validation (supporting), visualization (supporting), writing-review & editing (supporting); Osbel Almora conceptualization (lead), data curation (lead), formal analysis (lead), investigation (lead), methodology (lead), software (equal), supervision (equal), validation (lead), visualization (lead), writing-original draft (lead), writing-review & editing (lead).

## Notes

The authors declare no competing financial interest.

## ACKNOWLEDGMENTS

This work has received funding from the European Union's Horizon 2020 research and innovation program under the Photonics Public-Private Partnership ([www.photonics21.org](http://www.photonics21.org)) with the project PEROXIS under grant agreement N° 871336. We acknowledge Dr. Phil Calado, Dr. Piers Barnes, Dr. Mohammed Azzouzi, and Benjamin Hilton for developing Driffusion<sup>18</sup> and releasing it as open-source code.<sup>29</sup> We acknowledge Dr. Marian Chapran for electrode deposition. O.A. thanks the Spanish State Research Agency (Agencia Estatal de Investigación) for the Juan de la Cierva 2021 grant.

## REFERENCES

- (1) Birowosuto, M. D.; Cortecchia, D.; Drozdowski, W.; Brylew, K.; Lachmanski, W.; Bruno, A.; Soci, C. X-Ray Scintillation in Lead Halide Perovskite Crystals. *Sci. Rep.* **2016**, *6*, 37254.
- (2) Wei, H.; Fang, Y.; Mulligan, P.; Chuirazzi, W.; Fang, H.-H.; Wang, C.; Ecker, B. R.; Gao, Y.; Loi, M. A.; Cao, L.; Huang, J. Sensitive X-Ray Detectors Made of Methylammonium Lead Tribromide Perovskite Single Crystals. *Nat. Photonics* **2016**, *10*, 333–339.
- (3) Heiss, W.; Brabec, C. Perovskites Target X-Ray Detection. *Nat. Photonics* **2016**, *10*, 288–289.
- (4) Peng, J.; Xu, Y.; Yao, F.; Lin, Q. Thick-Junction Perovskite X-Ray Detectors: Processing and Optoelectronic Considerations. *Nanoscale* **2022**, *14*, 9636–9647.
- (5) Armaroli, G.; Ferlauto, L.; Lédée, F.; Lini, M.; Ciavatti, A.; Kovtun, A.; Borgatti, F.; Calabrese, G.; Milita, S.; Fraboni, B.; Cavalcoli, D. X-Ray-Induced Modification of the Photophysical Properties of MAPbBr<sub>3</sub> Single Crystals. *ACS Appl. Mater. Interfaces* **2021**, *13*, 58301–58308.
- (6) García-Battle, M.; Baussens, O.; Amari, S.; Zaccaro, J.; Gros-Daillon, E.; Verilhac, J.-M.; Guerrero, A.; Garcia-Belmonte, G. Moving Ions Vary Electronic Conductivity in Lead Bromide

Perovskite Single Crystals through Dynamic Doping. *Adv. Electron. Mater.* **2020**, *6*, 2000485.

(7) Chai, Y.; Juan, Z.; Wu, Y.; Liu, Y.; Li, X. Suppressing the Ion Migration in Halide Perovskite Wafers for Current-Drift Free X-Ray Detectors. *ACS Appl. Electron. Mater.* **2023**, *5*, 544–551.

(8) García-Battle, M.; Zia, W.; Aranda, C.; Saliba, M.; Almora, O.; Guerrero, A.; Garcia-Belmonte, G. Observation of Long-Term Stable Response in MAPbBr<sub>3</sub> Single Crystals Monitored through Displacement Currents under Varying Illumination. *Solar RRL* **2022**, *6*, 2200173.

(9) García-Battle, M.; Mayén Guillén, J.; Chapran, M.; Baussens, O.; Zaccaro, J.; Verilhac, J.-M.; Gros-Daillon, E.; Guerrero, A.; Almora, O.; Garcia-Belmonte, G. Coupling between Ion Drift and Kinetics of Electronic Current Transients in MAPbBr<sub>3</sub> Single Crystals. *ACS Energy Lett.* **2022**, *7*, 946–951.

(10) García-Battle, M.; Deumel, S.; Huerdler, J. E.; Tedde, S. F.; Almora, O.; Garcia-Belmonte, G. Effective Ion Mobility and Long-Term Dark Current of Metal-Halide Perovskites of Different Crystallinity and Composition. *Adv. Photonics Res.* **2022**, *3*, 2200136.

(11) Li, Z.; Zhou, F.; Yao, H.; Ci, Z.; Yang, Z.; Jin, Z. Halide Perovskites for High-Performance X-Ray Detector. *Mater. Today* **2021**, *48*, 155–175.

(12) O'Kane, S. E. J.; Richardson, G.; Pockett, A.; Niemann, R. G.; Cave, J. M.; Sakai, N.; Eperon, G. E.; Snaith, H. J.; Foster, J. M.; Cameron, P. J.; Walker, A. B. Measurement and Modelling of Dark Current Decay Transients in Perovskite Solar Cells. *J. Mater. Chem. C* **2017**, *5*, 452–462.

(13) Almora, O.; Miravet, D.; Gelmetti, I.; Garcia-Belmonte, G. Long-Term Field Screening by Mobile Ions in Thick Metal Halide Perovskites: Understanding Saturation Currents. *Phys. Status Solidi RRL* **2022**, *16*, 202200336.

(14) García-Battle, M.; Deumel, S.; Huerdler, J. E.; Tedde, S. F.; Guerrero, A.; Almora, O.; Garcia-Belmonte, G. Mobile Ion-Driven Modulation of Electronic Conductivity Explains Long-Timescale Electrical Response in Lead Iodide Perovskite Thick Pellets. *ACS Appl. Mater. Interfaces* **2021**, *13*, 35617–35624.

(15) Almora, O.; Matt, G. J.; These, A.; Kanak, A.; Levchuk, I.; Shrestha, S.; Osvet, A.; Brabec, C. J.; Garcia-Belmonte, G. Surface Versus Bulk Currents and Ionic Space-Charge Effects in CsPbBr<sub>3</sub> Single Crystals. *J. Phys. Chem. Lett.* **2022**, *13*, 3824–3830.

(16) Baussens, O.; Maturana, L.; Amari, S.; Zaccaro, J.; Verilhac, J.-M.; Hirsch, L.; Gros-Daillon, E. An Insight into the Charge Carriers Transport Properties and Electric Field Distribution of CH<sub>3</sub>NH<sub>3</sub>PbBr<sub>3</sub> Thick Single Crystals. *Appl. Phys. Lett.* **2020**, *117*, 041904.

(17) Deumel, S.; van Breemen, A.; Gelinck, G.; Peeters, B.; Maas, J.; Verbeek, R.; Shanmugam, S.; Akkerman, H.; Meulenkamp, E.; Huerdler, J. E.; Acharya, M.; García-Battle, M.; Almora, O.; Guerrero, A.; Garcia-Belmonte, G.; Heiss, W.; Schmidt, O.; Tedde, S. F. High-Sensitivity High-Resolution X-Ray Imaging with Soft-Sintered Metal Halide Perovskites. *Nat. Electron.* **2021**, *4*, 681–688.

(18) Calado, P.; Gelmetti, I.; Hilton, B.; Azzouzi, M.; Nelson, J.; Barnes, P. R. F. Driffusion: An Open Source Code for Simulating Ordered Semiconductor Devices with Mixed Ionic-Electronic Conducting Materials in One Dimension. *J. Comput. Electron.* **2022**, *21*, 960–991.

(19) Turedi, B.; Lintangpradipto, M. N.; Sandberg, O. J.; Yazmaciyan, A.; Matt, G. J.; Alsalloum, A. Y.; Almasabi, K.; Sakhatskiy, K.; Yakunin, S.; Zheng, X.; Naphade, R.; Nematulloev, S.; Yeddu, V.; Baran, D.; Armin, A.; Saidaminov, M. I.; Kovalenko, M. V.; Mohammed, O. F.; Bakr, O. M. Single-Crystal Perovskite Solar Cells Exhibit Close to Half a Millimeter Electron-Diffusion Length. *Adv. Mater.* **2022**, *34*, 2202390.

(20) Mott, G. R. NF, "Electronic Processes in Ionic Crystals". *J. Chem. Educ.* **1965**, *42*, A692.

(21) Shrestha, S.; Fischer, R.; Matt, G. J.; Feldner, P.; Michel, T.; Osvet, A.; Levchuk, I.; Merle, B.; Golkar, S.; Chen, H.; Tedde, S. F.; Schmidt, O.; Hock, R.; Rührig, M.; Göken, M.; Heiss, W.; Anton, G.; Brabec, C. J. High-Performance Direct Conversion X-Ray Detectors

Based on Sintered Hybrid Lead Triiodide Perovskite Wafers. *Nat. Photonics* **2017**, *11*, 436–440.

(22) Olyaeefar, B.; Ahmadi-Kandjani, S.; Asgari, A. Bulk and Interface Recombination in Planar Lead Halide Perovskite Solar Cells: A Drift-Diffusion Study. *Phys. E* **2017**, *94*, 118–122.

(23) Bertoluzzi, L.; Patel, J. B.; Bush, K. A.; Boyd, C. C.; Kerner, R. A.; O'Regan, B. C.; McGehee, M. D. Incorporating Electrochemical Halide Oxidation into Drift-Diffusion Models to Explain Performance Losses in Perovskite Solar Cells under Prolonged Reverse Bias. *Adv. Energy Mater.* **2021**, *11*, 2002614.

(24) Moia, D.; Gelmetti, I.; Calado, P.; Hu, Y.; Li, X.; Docampo, P.; de Mello, J.; Maier, J.; Nelson, J.; Barnes, P. R. F. Dynamics of Internal Electric Field Screening in Hybrid Perovskite Solar Cells Probed Using Electroabsorption. *Phys. Rev. Appl.* **2022**, *18*, 044056.

(25) Jia, S.; Xiao, Y.; Hu, M.; He, X.; Bu, N.; Li, N.; Liu, Y.; Zhang, Y.; Cui, J.; Ren, X.; Zhao, K.; Liu, M.; Wang, S.; Yuan, N.; Ding, J.; Yang, Z.; Liu, S. Ion-Accumulation-Induced Charge Tunneling for High Gain Factor in P–I–N-Structured Perovskite  $\text{CH}_3\text{NH}_3\text{PbI}_3$  X-Ray Detector. *Adv. Mater. Technol.* **2022**, *7*, 2100908.

(26) Bazant, M. Z.; Thornton, K.; Ajdari, A. Diffuse-Charge Dynamics in Electrochemical Systems. *Phys. Rev. E* **2004**, *70*, 021506.

(27) Almora, O.; Guerrero, A.; Garcia-Belmonte, G. Ionic Charging by Local Imbalance at Interfaces in Hybrid Lead Halide Perovskites. *Appl. Phys. Lett.* **2016**, *108*, 043903.

(28) Einstein, A. Über Die Von Der Molekularkinetischen Theorie Der Wärme Geforderte Bewegung Von in Ruhenden Flüssigkeiten Suspendierten Teilchen. *Ann. Phys.* **1905**, *322*, 549–560.

(29) Calado, P.; Barnes, P.; Gelmetti, I.; Azzouzi, M.; Hilton, B. Driftfusion. 2019, <https://github.com/barnesgroupLCL/Driftfusion> (accessed April 17, 2023).